eprints@whiterose.ac.uk
https://eprints.whiterose.ac.uk/

Optical-mode structure of micropillar microcavities containing a fluorescent conjugated polymer

Faleh Lafta Al-Jashaam[1,2], Rahul Jayaprakash[1], David Coles[1,3], Andrew J. Musser[1],

Kyriacos Georgiou[1] and David G. Lidzey[1*]

[1] Department of Physics and Astronomy, University of Sheffield, Sheffield, S3 7RH, U.K.

[2] Department of Physics, College of Science, Tikrit University, Iraq

[3] Ossila Ltd, Solpro Business Park, Windsor Street, Sheffield, S4 7WB, U.K.

* Author for correspondence: d.g.lidzey@sheffield.ac.uk

Abstract

We have explored light emission from a series of micropillar microcavities containing a fluorescent, red-emitting conjugated polymer. Cavities were fabricated by defining two dielectric mirrors either side of a polymer active region. Focused ion-beam lithography was then used to etch pillar structures into the planar cavity having diameters between 1 and 11 μm. The photoluminescence emission of the cavities is characterized using real-space tomographic and Fourier-space imaging techniques, with emission shown to be quantized into a mode-structure resulting from both vertical and lateral optical confinement within the pillar. We demonstrate that optical-confinement effects result in a blue-shift of the fundamental mode as the pillar diameter is reduced, with a model applied to describe the energy and distribution of the confined optical modes.

Keywords: Micropillar, microcavity, organic-semiconductor, conjugated-polymer,

mode-quantization.

By defining a pattern into a dielectric material at sub-micron length-scales, it is possible to create a structure that can confine photons within a localized volume and thus act as an optical cavity[1–5]. By depositing a light-emitting semiconductor within such a cavity, a range of effects can be engineered - for example within the so-called 'weak-coupling regime' it is possible to modify the local density of optical states such that the spontaneous emission rate can be modified via the Fermi Golden Rule (Purcell Factor)[6,7]. Such an approach is widely used in a range of advanced photonic devices; for example, planar resonant cavity light emitting diodes are structures in which an active emissive region is placed between two dielectric mirrors forming a 2-dimensional optical cavity[8–12]. Here, the resulting optical confinement can be used to enhance the intensity of emission from the semiconductor within the cavity and also control its emission color[13,14].

A higher level of photon confinement can be achieved in so-called micropillar structures. Such structures typically take the form of a 1-dimensional cylinder, in which an emissive material is positioned between two dielectric mirrors (see Figure 1(a)). Such structures are usually fabricated from a 2D resonant cavity structure that is then vertically etched following micro-patterning using electron-beam lithography. Micropillar structures achieve optical confinement both parallel to the pillar axis (by in-phase reflection from the dielectric mirrors) and normal to the pillar axis through total internal reflection due to the large difference in refractive index[15]. The high level of sophistication achievable using inorganic semiconductor processing techniques has allowed micropillar structures to be realized having very high quality (Q) factors[16], with recent pillar-structures demonstrated having Q-factors in excess of 250,000[17]. This strong confinement can be used to engineer enhancements in spontaneous emission rates (the Purcell Factor)[18–20], and thus by placing a single quantum emitter in a micropillar, a device can be created that acts as a source of near indistinguishable single photons[21]. For this reason, micropillar structures and devices are now being explored

as practical systems for 'single-photons on demand' in quantum-cryptography technologies[22,23]. Micropillar structures also allow a range of phenomena to be explored, including strong coupling between single photons and a single quantum-dot[24,25] and the realization of low-threshold polariton lasing[26].

In contrast to inorganic semiconductors, organic semiconductors combine the advantages of strongly-bound excitons having high oscillator strength which survive to room temperature[27], high fluorescence quantum efficiency[28] and ease of processing into thin-film light-emitting devices[29]. There is thus growing interest in the development of micropillar structures in which the active material is based on an organic semiconductor. Here, Adawi et al first reported the fabrication of a micropillar microcavity containing a fluorescent molecular dye using an ion-beam etching technique[30]. Using near-field optical imaging techniques, it was shown that such structures were able to modify spontaneous emission rates. Organic micropillars have also previously been fabricated using a thermal imprint technology to pattern a liquid-crystalline molecular dye into pillar shapes on the surface of a dielectric mirror[31]. By coating such structures with a thin film of gold, the hemispherical pillar-geometry cavities created were shown to support several families of quantized optical modes. Other work has used an optical writing technique to selectively change the refractive index of a thin film of a biologically produced fluorescent protein by photobleaching[32]. Such films were then used as the active layer of a micropillar, with lateral photonic confinement leading to a reduction in lasing thresholds compared to an un-patterned control. Further approaches to fabrication of laterally quantized states in organic photonic structures include the use of advanced shadow-masking techniques[33]. Conjugated polymers operating in the strong-coupling regime have also been engineered into microcavities containing a zero-dimensional Gaussian defect, fabricated by focused ion-beam milling[34]. Such structures have been shown to undergo

polariton condensation at high excitation density and are of interest as analogue quantum simulators.

In this paper, we have explored the optical structure of a micropillar containing a thin film of a highly fluorescent red-emitting conjugated polymer. Following our previous methodology [30] using a focused ion beam (FIB) to directly pattern a planar cavity, we have created a series of different diameter micropillar structures characterized by a number of optical modes. We make a significant advancement on our previous work [30] to image the luminescence from such structures using both real-space and Fourier-techniques and develop an optical model to provide a comprehensive description of the cavity mode structure. In contrast to our previous work in which no optical mode structure was observed [30], we believe that this is one of the first examples of the use of a high-resolution tomographic imaging technique being applied to create a real space image of the confined optical modes in an organic photonic device[35]. We emphasize that the polymer used in our cavities is typical of many conjugated organic semiconductors used to create high-efficiency light emitting diodes, and thus our work represents a step towards the development of new types of electrically-driven light sources. Importantly, the techniques used here could be used to create lattices of micropillars in which there is a delocalized band-structure within the plane of the substrate. Such systems are currently receiving significant interest as structures in which there is unidirectional flow of a polariton wavepacket around the edge of the lattice, forming a topological insulator[36].

A schematic of the micropillars fabricated is shown in Figure 1(a). To create these structures, a dielectric mirror (Distributed Bragg Reflector [DBR]) consisting of 8.5 quarter-wave pairs of TiO_2 and SiO_2 was first deposited on a quartz substrate. This DBR was designed to have a center-wavelength of 660 nm to coincide with the peak of the fluorescence of the organic semiconductor. Here, all dielectric films were deposited using electron-beam

evaporation from TiO_2 and SiO_2 target materials that were placed in graphite crucibles. The growth of the individual layers in the DBR was monitored using a quartz-crystal microbalance (deposition rates maintained at 2 Ås^{-1}), with each TiO_2 and SiO_2 layer having a thickness of 68.6 and 100.9 nm respectively. The reflectivity of a DBR consisting of TiO_2 / SiO_2 mirror pairs is shown in Figure 1(b) along with its simulation at normal incidence, obtained using a standard transfer matrix model. As is can be seen, the reflectivity stop-band extends from 546 nm to 734 nm, with the maximum mirror reflectivity being around 96% at 660 nm.

A 195 nm thick film of the polymer PFR was then spin-cast onto this DBR from a dichlorobenzene solvent. PFR was chosen as it has a high fluorescence quantum efficiency of around 45% and emits luminescence that peaks around 650 nm. Figures 2(a) and (b) show the chemical structure of PFR and its UV-Vis absorbance and fluorescence emission respectively. As can be seen, the peak of the PFR emission approximately coincides with the center of the DBR stop-band. A second DBR was then deposited onto the surface of the PFR film, forming a planar microcavity. The thickness of the layer pairs in this top mirror (determined from transfer matrix reflectivity simulations of the full cavity stack) were slightly different from those of the bottom mirror (8.5 pairs TiO_2 (75 nm) / SiO_2 (110.2 nm) caused as a result of a slight change in the deposition parameters between different coating runs. Transfer matrix modelling indicates that the cavity created supported a λ / 2 mode around 650 nm, with the cavity having an EM field antinode positioned in the center of the PFR active layer.

Before fabricating the planar cavity into micropillars, we have firstly characterized the optical properties of the un-patterned cavity. This is shown in Figures 3(a) and (b) respectively where we plot white-light reflectivity and photoluminescence emission (PL) recorded as a function of angle. Here, measurements were made using a goniometer system, which used a series of lenses to deliver or collect light from the cavity surface that were coupled to optical fibers. White light (for reflectivity measurements) was generated using a fiber-coupled

deuterium halogen lamp, with luminescence generated using light at 405 nm from a Thorlabs continuous-wave laser diode. In all cases, spectral measurements were made using a fiber-coupled Andor Shamrock SR-303i-A triple-grating imaging spectrograph, with a focal length of 0.303m. The spectra were recorded using a 300 grooves / mm grating blazed at 500 nm. Note that the smallest angle at which white light reflectivity could be measured was 12°, although PL emission could be recorded at all angles including normal incidence.

It can be seen (Figure 3(a)) that the white-light reflectivity is characterized by a broad stop-band onto which a sharp dip is apparent, a feature that corresponds to the cavity mode. This mode has a strong angular dispersion which we can fit using a transfer-matrix model (dashed line). We find that the PL emission (Figure 3(b)) undergoes a similar angular-dependent dispersion, however emission is approximately concentrated over the angular / wavelength range 0 - 50° (675 – 600 nm). This angular / wavelength range is in fact defined by the emission properties of the PFR, which emits PL at wavelengths longer than approximately 575 nm. Interestingly, we observe some TE/TM polarization splitting of the cavity emission, with this effect observed both in reflectivity and in emission.

We have used such planar cavities to construct micropillar devices. Here, a FEI quanta 200 3D ion-beam lithography system was used to write a series of micropillar structures into the cavity surface (see Figure 4(a)). This was done using a 30 keV beam of Ga ions that was directed to the microcavity surface at normal incidence to write circular trenches having a depth of 5 μm and a width of 1 μm, creating a series of micropillars having diameters between 1 and 11 μm. To avoid charging the surface of the sample during ion-beam writing, the planar microcavity was coated with a 10 nm thin film of gold. This gold film remained on the micropillar surface, with a transfer-matrix model indicating that it slightly attenuated the PL emitted by the structure by around 16%. An SEM image of a typical micropillar (in this case having a diameter of 11 μm) is shown in Figure 4(b).

We have characterized the emission from our cavities using a 405 nm semiconductor laser that was focused onto the sample surface in a spot having diameter of 10 μm. The emitted PL from the micropillars and some of the surrounding un-patterned cavity was collected through a 0.7 NA lens and directed into a 0.25 m nitrogen-cooled charge-coupled device (CCD) spectrometer having a spectral resolution of 0.5 Å, with all measurements performed in air and at room temperature. Here, the use of high NA lens collects all light emitted in a forward cone of ± 44.4°. Photoluminescence emission from an un-patterned region of the cavity is shown in Figure 5(a) together with emission from pillars having a diameter of 4, 6 and 7 μm. When this unpatterned cavity is etched into a micropillar, we find a significant evolution in emission pattern, with emission now characterized by a series of sharp peaks having a typical FWHM linewidth of 2 nm. We focus our attention on these diameter micropillars, as our simulations suggest that the mode separation in larger diameter structures becomes smaller than the linewidth of the individual modes and is thus unresolvable. We also find that there is significant broadening of the optical modes in micropillars having a diameter of less than 4 μm; an effect that most likely originates from roughness in the micropillar walls (*vide infra*). In the figure, it can be seen that the fundamental mode undergoes a progressive blue-shift as pillar diameter is reduced. We also find that as pillar diameter is reduced from 7 to 4 μm, the spacing between adjacent modes increases, with the fundamental cavity mode undergoing a blue shift of around 5.1 nm.

To gain further insight into the origin of the optical modes observed in the spectra shown in Figure 5, we have performed Fourier-space (k-space) imaging of the pillar emission. This technique permits the energy dispersion of emission to be characterized in a single measurement by projecting the Fourier-image of the pillar directly onto the slits of a spectrometer (Andor Shamrock SR-303i-A). This was achieved by placing a Fourier plane imaging lens between the objective (Edmund Optics 20X, NA = 0.6) and the final collection

lens. It should be noted that the real-space image has been spatially filtered to extract k-space emission from just the pillar and reject emission from the surrounding unpatterned cavity region.

Typical energy-angle dependent photoluminescence dispersion data recorded from an unpatterned cavity region is shown in Fig 5(b), with emission from 4, 6 and 7 μm diameter pillars shown in Figures 5(c), (d) and (e) respectively. We can use the emission dispersion curve of the unpatterned cavity (Figure 5(b)) to determine the cavity Q-factor. Here, we find that the PL emission linewidth at $k = 0$ is 1.3 nm, corresponding to a cavity Q-factor of ~ 520; a value that compares closely with a theoretical (transfer matrix model) prediction of ~ 586. On etching the planar cavity into micropillars, it can be seen that the cavity mode dispersion is characterized by a series of optical modes having an approximately parabolic dispersion. As the diameter of the micropillars are reduced, we find that emission is dominated by two discrete modes that are evident between 662 and 665 nm (corresponding to angles 0 to ± 10°), together with a series of modes that are less well defined that exist at higher energy.

We have also performed real-space tomographic imaging of the pillar emission using a slight modification of the Fourier-space imaging setup described above. Here an additional lens was placed between the imaging and final collection lenses, forming two telescopes that result in an overall magnification of 113X. By scanning the piezo-controlled final collection lens across the spectrometer slits (x-axis), and by extracting intensity data from pixels along the CCD columns (y-axis) we can precisely map the real-space energy distribution of the emission and thus energetically map the optical mode-structure of the pillars.

A series of real-space tomographic images recorded from a 4 μm pillar at wavelengths corresponding to four distinct modes are shown in Figure 6(a). From a comparison to the k-space distribution and modelling (see below) we assign these modes as $E_{0,1}$, $E_{1,1}$, $E_{0,2/2,1}$, and $E_{3,1}$. The fundamental mode is centered on the middle of the micropillar, although it is found

to be slightly asymmetric. This asymmetry is most likely attributed to a slight ellipticity arising from the FIB etching of the planar cavity; an effect that is also evident in the $E_{1,1}$ mode. By contrast, the higher order modes have larger mode volume and appear less affected by the slight ellipticity of the pillar. We note that the mode labelled $E_{0,2/2,1}$ is in fact a combination of two distinct modes (a four-lobed structure around the pillar perimeter and a single peak in the pillar center) that are too close in energy to be separately resolved by our system. In the $E_{3,1}$ mode most emission occurs from the perimeter of the pillar and can thus be assigned to a whispering-gallery mode.

To understand the origin of these modes, we have modelled the cavities using Schrödinger's equation for a particle in an infinite circular well, which in the relevant polar coordinates is given by

$$-\frac{\hbar^2}{2\mu}\left(\frac{\delta^2}{\delta r^2} + \frac{1}{r}\frac{\delta}{\delta r} + \frac{1}{r^2}\frac{\delta^2}{\delta\theta^2}\right)\psi(r,\theta) = E\psi(r,\theta) \qquad\qquad 1$$

Here, $\psi(r,\theta)$ corresponds to the real-space wavefunctions, E to their respective eigenenergies and μ the effective mass of a photon which is $\sim 10^{-5}m_o$ (where m_o is the effective mass of an electron). Taking into account appropriate boundary conditions defined by the cavity geometry, equation (2) summarizes the energy of the various confined optical states within the cavity.

$$E_{(m,n_r)} = \frac{\hbar^2}{2\mu R^2}\left(z_{(m,n_r)}\right)^2 \qquad\qquad 2$$

Here m is the azimuthal quantum number, n_r is the radial quantum number, R is the radius of the circular well and $z_{(m,n_r)}$ is the n_r-th zero of the regular Bessel function $J_m(z)$. The wavefunction of the various azimuthal and radial modes is then given by

$$\psi_{(m,n_r)}(r,\theta) = N_{(m,n_r)} J_m\left(\frac{z_{(m,n_r)}}{R}r\right)e^{im\theta} \qquad\qquad 3$$

where $N_{(m,n_r)}$ is a normalization factor calculated using

$$2\pi N^2_{(m,n_r)} \int_0^R J_m^2\left(\frac{z_{(m,n_r)}}{R}r\right)r\,dr = 1 \qquad\qquad 4$$

The wavefunction in Fourier space is then obtained by integrating the wavefunctions in real-space using

$$\psi_{(m,n_r)}(k) = \int \psi_{(m,n_r)}(r,\theta)\, e^{i(k_x r cos(\theta))} r\,dr\,d\theta \qquad\qquad 5$$

where k is the wavevector. This yields the following solutions of the circular micropillar.

$$\psi_{(m,n_r)}(k_x) = N_{(m,n_r)} \frac{J_m(k_x R)}{z^2_{(m,n_r)}-k_x R^2} \qquad\qquad 6$$

The spatial distribution of the modes calculated using the model are plotted in Figure 6(b). It can be seen that there is an excellent match to the real-space tomographic measurements, both in mode distribution and energetic position. We superimpose the calculated energies of the various modes onto the dispersion data shown in Figure 6(c) (note that we only plot the energy levels of optical modes that are observed experimentally. It can be seen that most of the micropillar emission corresponds to modes $E_{0,1}$ and $E_{1,1}$ which are predominantly localized within the center of the pillar, with faint signatures at higher energy being seen of modes having higher azimuthal and radial quantum number. This observation most likely indicates that modes that are closer to the pillar walls are more likely to suffer from scattering-induced loss

mechanisms as a result of roughness caused by the focused-ion beam lithography process. Indeed, we find that the measured Q-factor of modes $E_{0,1}$, $E_{1,1}$ and $E_{3,2}$ is 257, 193 and 174 respectively, indicating a greater degree of optical loss than is experienced by the fundamental mode.

The simulated Fourier space distributions of the different energy levels are shown in Figure 6(d) along with measured cross sections of the PL dispersion corresponding to energy levels $E_{0,1}$ and $E_{1,1}$ (note that the various modes are displaced vertically for the sake of clarity and are not plotted on a common energy scale). It can be seen that we see a slight discrepancy between the experimental and theoretical distribution of emission from mode $E_{1,1}$. Our model indicates that this discrepancy results from a slight asymmetry caused by the ellipticity of the pillar; a conclusion in accord with the real-space images shown in Figure 6(a).

In summary, we have fabricated micropillar structures that contain a red-fluorescent conjugated polymer. We have characterized the optical mode structure of such pillars using combined white-light reflectance and photoluminescence emission (recorded using both far-field and Fourier-space imaging techniques). Optical modelling of the pillar emission can successfully describe the distribution of the cavity modes, with modes localized towards the center of the pillar dominating the emission. The fabrication of such structures based on the use of focused ion-beam now presents an exciting opportunity to explore polaritonic effects in micropillars. We have already shown that molecular dyes dispersed into a polymeric matrix undergo strong-coupling and lasing[37] when fabricated into a 2-dimensional (planar) microcavity. It will be interesting to utilize such material systems in a micropillar to explore whether polariton condensation and lasing thresholds can be reduced. Furthermore, organic semiconductors can also be diluted into an inert matrix at low concentration, allowing single chromophore emission to be identified from spatially-separated molecules[38,39]. If such single-chromophore emitting films were placed in a micropillar, it would potentially offer a route to

creating high repetition-rate, single-photon light sources that operate at room-temperature. Finally, we see significant opportunities to study optical-band structure within two-dimensional lattices of such micropillar structures.

References

[1]   K. J. Vahala, *Nature* **2003**, *424*, 839.

[2]   M. S. Skolnick, T. A. Fisher, D. M. Whittaker, *Semicond. Sci. Technol.* **1998**, *13*, 645.

[3]   D. G. Lidzey, D. D. C. Bradley, M. S. Skolnick, T. Virgili, S. Walker, D. M. Whittaker, *Lett. to Nat.* **1998**, *395*, 53.

[4]   A. Dodabalapur, L. J. Rothberg, R. H. Jordan, T. M. Miller, R. E. Slusher, J. M. Phillips, *J. Appl. Phys.* **1996**, *80*, 6954.

[5]   D. Bajoni, *J. Phys. D. Appl. Phys.* **2012**, *45*, 313001.

[6]   C. Weisbuch, H. Benisty, R. Houdre, *J. Lumin.* **2000**, *85*, 271.

[7]   R. J. Barbour, P. A. Dalgarno, A. Curran, K. M. Nowak, H. J. Baker, D. R. Hall, N. G. Stoltz, P. M. Petroff, R. J. Warburton, *J. Appl. Phys.* **2011**, *110*, 053107.

[8]   E. F. Schubert, Y.-H. Wang, A. Y. Cho, L.-W. Tu, G. J. Zydzik, *Appl. Phys. Lett.* **1992**, *60*, 921.

[9]   A. J. Shaw, A. L. Bradley, J. F. Donegan, J. G. Lunney, *IEEE Photonics Technol. Lett.* **2004**, *16*, 2006.

[10]   J. Dorsaz, J.-F. Carlin, C. M. Zellweger, S. Gradecak, M. Ilegems, *Phys. Status Solidi Appl. Res.* **2004**, *201*, 2675.

[11] A. M. Adawi, L. G. Connolly, D. M. Whittaker, D. G. Lidzey, E. Smith, M. Roberts, F. Qureshi, C. Foden, N. Athanassopoulou, *J. Appl. Phys.* **2006**, *99*, 054505.

[12] V. Bulović, V. Khalfin, G. Gu, P. Burrows, D. Garbuzov, S. R. Forrest, *Phys. Rev. B - Condens. Matter Mater. Phys.* **1998**, *58*, 3730.

[13] M. J. Park, G. H. Kim, Y. H. Son, H. W. Bae, J. H. Kong, J. H. Kwon, *Opt. Express* **2014**, *22*, 19919.

[14] C. Xiang, W. Koo, F. So, H. Sasabe, J. Kido, *Light Sci. Appl.* **2013**, *2*, e74.

[15] S. Reitzenstein, A. Forchel, *J. Phys. D. Appl. Phys.* **2010**, *43*, 033001.

[16] S. Reitzenstein, C. Hofmann, A. Gorbunov, M. Strauß, S. H. Kwon, C. Schneider, A. Löffler, M. Kamp, S. Höfling, A. Forchel, *Appl. Phys. Lett.* **2007**, *90*, 251109.

[17] C. Schneider, P. Gold, S. Reitzenstein, S. Höfling, M. Kamp, *Appl. Phys. B* **2016**, *122*, 19.

[18] J. M. Gérard, B. Sermage, B. Gayral, B. Legrand, E. Costard, V. Thierry-Mieg, *Phys. Rev. Lett.* **1998**, *81*, 1110.

[19] T. Jakubczyk, W. Pacuski, T. Smoleński, A. Golnik, M. Florian, F. Jahnke, C. Kruse, D. Hommel, P. Kossacki, *Appl. Phys. Lett.* **2012**, *101*, 132105.

[20] M. Bayer, T. L. Reinecke, F. Weidner, A. Larionov, A. McDonald, A. Forchel, *Phys. Rev. Lett.* **2001**, *86*, 3168.

[21] X. Ding, Y. He, Z.-C. Duan, N. Gregersen, M.-C. Chen, S. Unsleber, S. Maier, C. Schneider, M. Kamp, S. Höfling, C.-Y. Lu, J.-W. Pan, *Phys. Rev. Lett.* **2016**, *116*, 020401.

[22] A. K. Nowak, S. L. Portalupi, V. Giesz, O. Gazzano, C. Dal Savio, P.-F. Braun, K. Karrai, C. Arnold, L. Lanco, I. Sagnes, A. Lemaître, P. Senellart, *Nat. Commun.* **2014**, *5*, 3240.

[23] C. Böckler, S. Reitzenstein, C. Kistner, R. Debusmann, A. Löffler, T. Kida, S. Höfling,

A. Forchel, L. Grenouillet, J. Claudon, J. M. Gérard, *Appl. Phys. Lett.* **2008**, *92*, 091107.

[24]   J. P. Reithmaier, G. Sek, A. Löffler, C. Hofmann, S. Kuhn, S. Reitzenstein, L. V Keldysh, V. D. Kulakovskii, T. L. Reinecke, A. Forchel, *Nature* **2004**, *432*, 197.

[25]   K. Hennessy, A. Badolato, M. Winger, D. Gerace, M. Atatüre, S. Gulde, S. Fält, E. L. Hu, A. Imamoğlu, *Nature* **2007**, *445*, 869.

[26]   D. Bajoni, P. Senellart, E. Wertz, I. Sagnes, A. Miard, A. Lemaître, J. Bloch, *Phys. Rev. Lett.* **2008**, *100*, 047401.

[27]   G. D. Scholes, G. Rumbles, *Nat. Mater.* **2006**, *5*, 683.

[28]   Y. Kawamura, K. Goushi, J. Brooks, J. J. Brown, H. Sasabe, C. Adachi, *Appl. Phys. Lett.* **2005**, *86*, 071104.

[29]   P. K. Bhatnagar, In *Nanomaterials and Their Applications*; Khan, Z. H., Ed.; 2018; pp. 261–287.

[30]   A. M. Adawi, A. Cadby, L. G. Connolly, W.-C. Hung, R. Dean, A. Tahraoui, a. M. Fox, a. G. Cullis, D. Sanvitto, M. S. Skolnick, D. G. Lidzey, *Adv. Mater.* **2006**, *18*, 742.

[31]   M. Dusel, S. Betzold, S. Brodbeck, S. Herbst, F. Würthner, D. Friedrich, B. Hecht, S. Höfling, C. P. Dietrich, *Appl. Phys. Lett.* **2017**, *110*, 201113.

[32]   C. P. Dietrich, M. Karl, J. Ohmer, U. Fischer, M. C. Gather, S. Höfling, *Adv. Mater.* **2017**, *29*, 1605236.

[33]   M. Langner, R. Gehlhaar, C. Schriever, H. Fröb, V. G. Lyssenko, K. Leo, *Appl. Phys. Lett.* **2007**, *91*, 181119.

[34]   F. Scafirimuto, D. Urbonas, U. Scherf, R. F. Mahrt, T. Stöferle, *ACS Photonics* **2018**, *5*, 85.

[35]   D. Urbonas, T. Stöferle, F. Scafirimuto, U. Scherf, R. F. Mahrt, *ACS Photonics* **2016**, *3*, 1542.

[36]   S. Klembt, T. H. Harder, O. A. Egorov, K. Winkler, R. Ge, M. A. Bandres, M.

Emmerling, L. Worschech, T. C. H. Liew, M. Segev, C. Schneider, S. Höfling, *Nature* **2018**, *562*, 552.

[37]   T. Cookson, K. Georgiou, A. Zasedatelev, R. T. Grant, T. Virgili, M. Cavazzini, F. Galeotti, C. Clark, N. G. Berloff, D. G. Lidzey, P. G. Lagoudakis, *Adv. Opt. Mater.* **2017**, *5*, 1700203.

[38]   B. Lounis, M. Orrit, *Reports Prog. Phys.* **2005**, *68*, 1129.

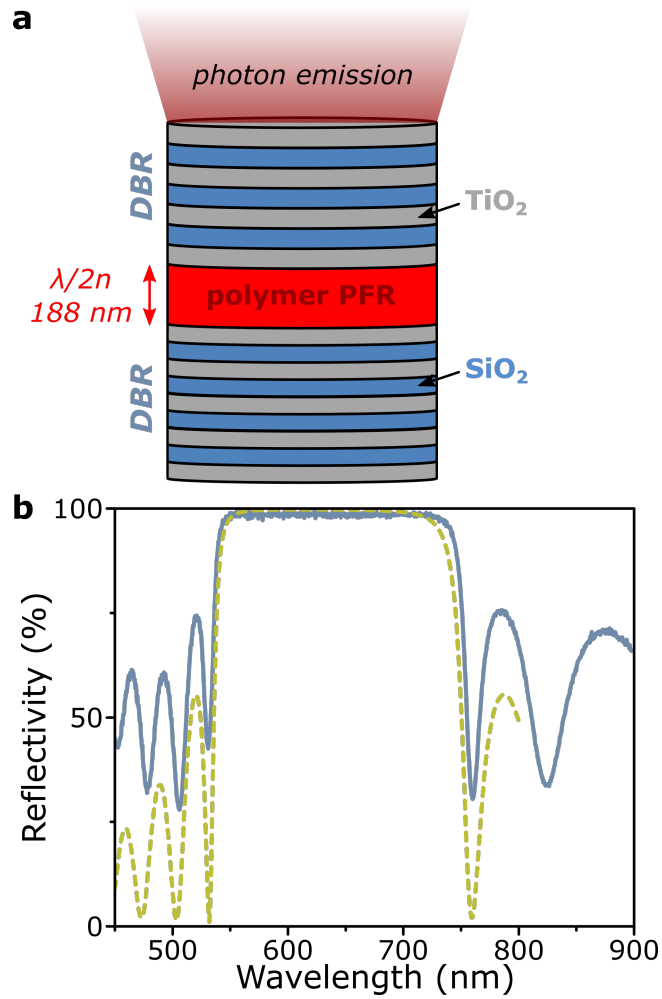[39]   J. M. Lupton, *Adv. Mater.* **2010**, *22*, 1689.

Figure 1| Dielectric cavity structure. a Schematic of micropillar cavity. The distributed Bragg reflectors (DBRs) consist of alternating λ/4n-thick layers of dielectric materials with contrasting index of refraction, where λ is the center of the mirror stop-band. The active layer is a pure spin-cast film of PFR. The micropillar geometry shown is etched into the full planar structure after fabrication. **b** Reflectivity spectrum of the bottom DBR along with its simulation.
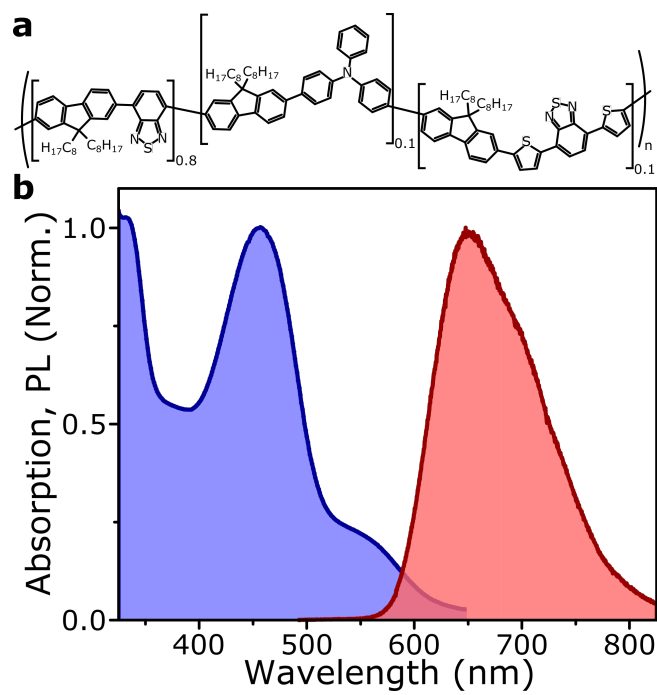
Figure 2| Active material PFR. a Chemical structure of PFR and **b** its absorption (blue) and

photoluminescence (red) spectra.

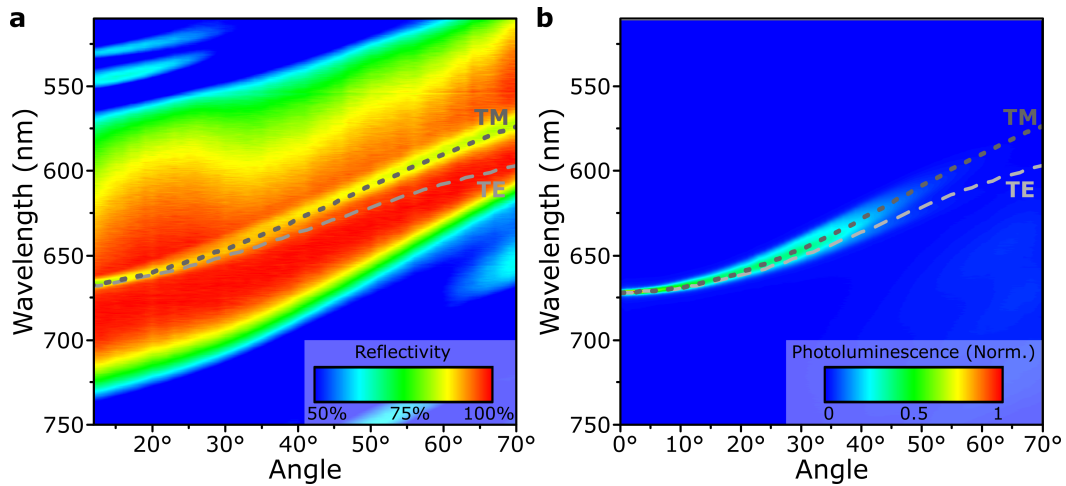**Figure 3| Planar cavity characteristics. a** Angle-resolved reflectivity of the unpatterned full cavity (DBR-PFR-DBR). The confined cavity mode is evident as a dip in the reflectivity in the center of the DBR stop-band **b** Angle-resolved photoluminescence of the unpatterned full cavity. The emission is limited to the spectral range 600-675 nm, constrained by the overlap of the cavity mode with the PFR film emission spectrum. In both cases the cavity dispersion is reproduced in transfer matrix modelling (dashed lines), where a TE/TM splitting can be observed at higher angles.
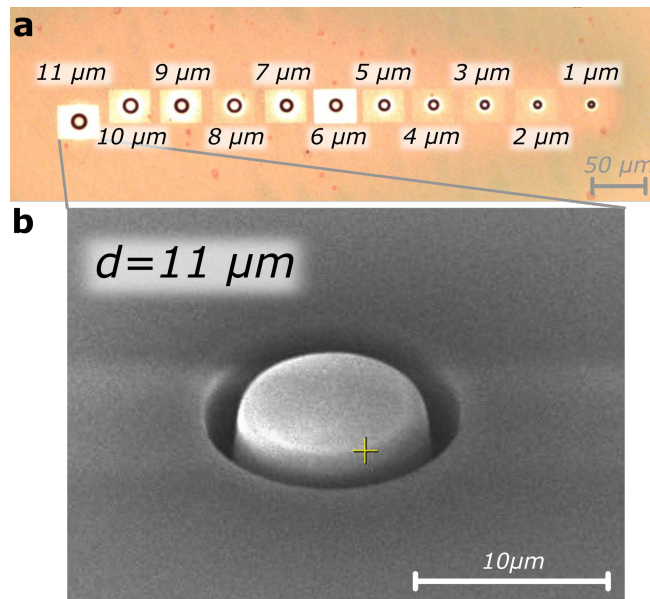
Figure 4| Micropillar array. a Optical microscope image of micropillars etched out of the full planar cavity, with cavity diameters indicated. **b** SEM image of a micropillar with a diameter of 11 μm.
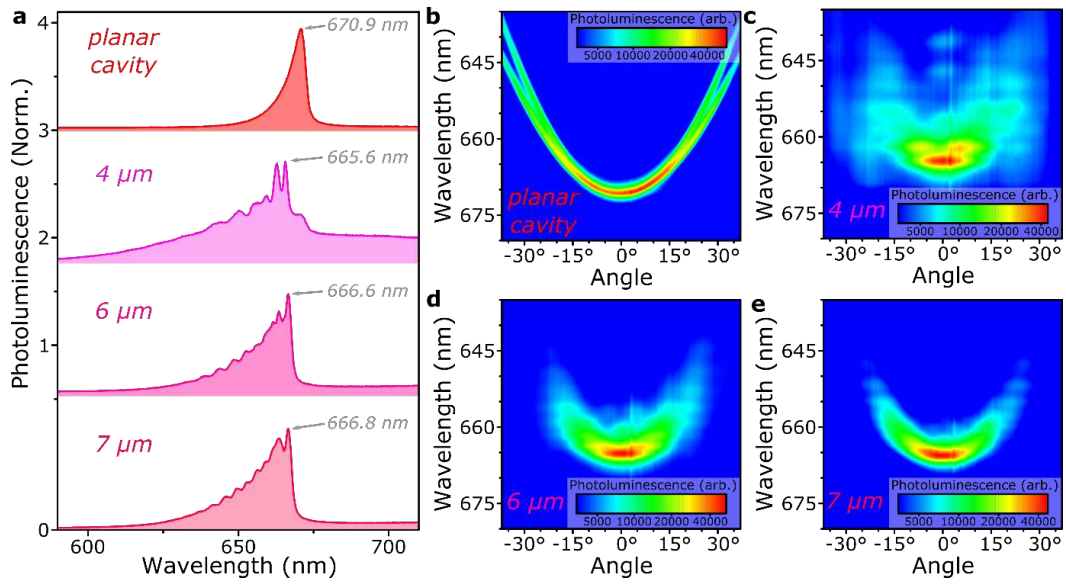
Figure 5| Additional confined modes. a Integrated emission from an unpatterned region of the cavity ('planar cavity') and three micropillars, revealing significant additional structure due to 1-dimensional confinement. The gradual blue-shift of the primary cavity mode with reducing diameter is highlighted. **b** Fourier-space imaging of photoluminescence from the unpatterned region reveals no structure aside from TE/TM splitting at high angles. Equivalent measurements on **c** 4 µm, **d** 6 µm and **e** 7 µm micropillars reveal finer mode structure. Emission through additional modes is particularly evident in 4 µm micropillars.
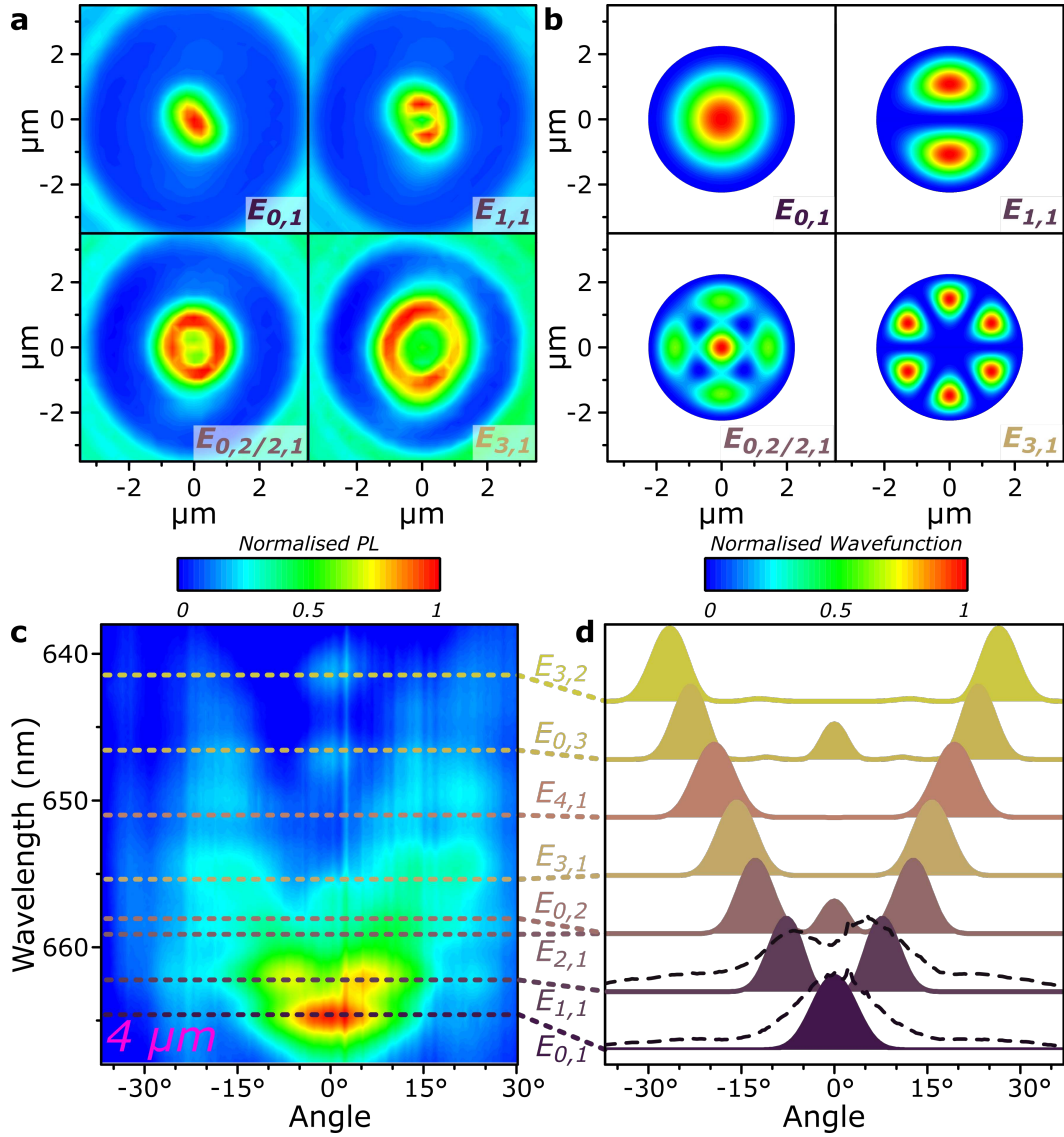
Figure 6| Real- and Fourier-space distributions of micropillar modes. a Real-space tomographic images of the 4 μm micropillar, measured at 664.8 ± 1 nm ($E_{0,1}$), 662.6 ± 1 nm ($E_{1,1}$), 658.3 ± 1 nm ($E_{0,2/2,1}$) and 654.4 ± 1 nm ($E_{3,1}$). The emission intensity corresponds directly to distribution of the confined optical modes within the pillar. **b** Corresponding calculated real-space distribution of the various confined modes. The micropillar center is at the origin in parts a and b. **c** Fourier-space image of the 4 μm micropillar, reproduced from Figure 5c. Dashed lines indicate the calculated energy of the various optical modes in the structure (see text for details). It can be seen that emission is dominated by the $E_{0,1}$ and $E_{1,1}$ modes. **d** Calculated Fourier-space distribution of each mode along with measured cross-

sections of the PL dispersion corresponding to energy levels $E_{0,1}$ and $E_{1,1}$. The various modes are displaced vertically for the sake of clarity.